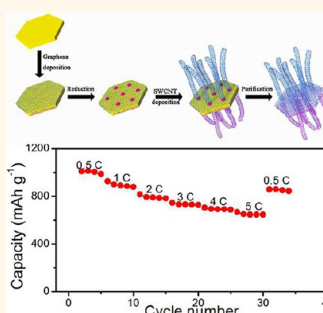# Graphene/Single-Walled Carbon Nanotube Hybrids: One-Step Catalytic Growth and Applications for High-Rate Li–S Batteries

Meng-Qiang Zhao,[†] Xiao-Fei Liu,[†,‡] Qiang Zhang,*,[†] Gui-Li Tian,[†] Jia-Qi Huang,[†] Wancheng Zhu,[‡] and Fei Wei*,[†]

[†]Beijing Key Laboratory of Green Chemical Reaction Engineering and Technology, Department of Chemical Engineering, Tsinghua University, Beijing 100084, China and [‡]Department of Chemical Engineering, Qufu Normal University, Shandong 273165, China

ABSTRACT The theoretically proposed graphene/single-walled carbon nanotube (G/SWCNT) hybrids by placing SWCNTs among graphene planes through covalent C—C bonding are expected to have extraordinary physical properties and promising engineering applications. However, the G/CNT hybrids that have been fabricated differ greatly from the proposed G/SWCNT hybrids because either the covalent C—C bonding is not well constructed or only multiwalled CNTs/carbon nanofibers rather than SWCNTs are available in the hybrids. Herein, a novel G/SWCNT hybrid was successfully fabricated by a facile catalytic growth on layered double hydroxide (LDH) at a high temperature over 950 °C. The thermally stable Fe nanoparticles and the uniform structure of the calcined LDH flakes are essential for the simultaneously catalytic deposition of SWCNTs and graphene. The SWCNTs and the CVD-grown graphene, as well as the robust connection between the SWCNTs and graphene, facilitated the construction of a high electrical conductive pathway. The internal spaces between the two stacked graphene layers and among SWCNTs offer room for sulfur storage. Therefore, the as obtained G/SWCNT-S cathode exhibited excellent performance in Li—S batteries with a capacity as high as 650 mAh g^{-1} after 100 cycles even at a high current rate of 5 C. Such a novel G/SWCNT hybrid can serve not only as a prototype to shed light on the chemical principle of G/CNT synthesis but also as a platform for their further applications in the area of nanocomposites, heterogeneous catalysis, drug delivery, electrochemical energy storage, and so on.

KEYWORDS: graphene · single-walled carbon nanotubes · lithium—sulfur battery · energy storage · hybrid materials

Single-walled carbon nanotubes (SWCNTs) are considered as the high end for carbon nanotube (CNT) technology because they have much better intrinsic properties when compared with multiwalled CNTs (MWCNTs), such as higher specific surface area (SSA), lower defect density, and tunable electronic characteristics according to their chirality.[1] However, the performance of SWCNTs in large-volume applications, such as fillers for nanocomposites, transparent conductive films, and electrode materials for energy storage, is always limited by problems of dispersion, anisotropy, and strong interface resistance between SWCNTs resulting from their one-dimensional (1D) structure and nanoscale size.[2,3] With the rapid rise of graphene in recent years, a three-dimensional (3D) hybrid structure constructed by placing SWCNTs among graphene planes

through covalent C—C bonding was proposed to solve the above-mentioned problems.[4,5] Graphene, which is a two-dimensional (2D) and one-atomic-thick sp^2 carbon layer, shares many similar properties with SWCNTs since the SWCNTs can be considered as a graphene cylinder rolled at a certain angle.[6] Therefore, combining the 1D SWCNTs and 2D graphene into 3D G/SWCNT hybrids is considered to be an effective route to bridge microscopic SWCNTs as well as graphene and macroscopic devices through a bottom-up strategy to further extend their applications without introducing any noncarbon impurities. The SWCNTs and graphene can be well dispersed in the G/SWCNT hybrids and effectively connected with reduced interface thermal and electrical resistances. Therefore, many excellent features of the G/SWCNT hybrids, such as thermal, mechanical, and

energy storage properties, have been proposed by theoretical modeling.[4,5] Controllable fabrication of the G/SWCNT hybrids is the first step in their realistic applications.

Up to now, several strategies have been explored to fabricate G/CNT hybrids, including postorganization methods through layer-by-layer self-assembly,[7−12] electrodeposition,[13] liquid phase reaction,[14,15] and direct chemical vapor deposition (CVD) growth routes through growing CNTs on graphene layers[16−21] and in situ growth of G/CNT hybrids on Cu foil coated with an Fe catalyst layer.[22] However, it should be noted that the postorganization methods cannot provide the covalent C−C bonding between graphene and CNTs. On the other hand, the direct growth routes for the fabrication of G/CNT hybrids show advantages in providing the possibility for the formation of a covalent C−C bonding connection, the growth of CNTs on graphene planes to enhance the dispersion of graphene, and the integration of high-quality CVD-grown graphene layers. However, one of the major drawbacks of these methods was the unstable catalyst nanoparticles (NPs) on graphene or metal substrates for CNT growth during CVD. As a result, only MWCNTs and carbon nanofibers were available for the as-fabricated G/CNT hybrids in these investigations.[16−23] The proposed G/SWCNT hybrids are still not available for realistic applications. Fabrication of G/SWCNT hybrids with covalent C−C bonding connections is still a great challenge for nanoscience and nanotechnology.

Generally, the CVD growth of SWCNTs requires catalyst NPs with small size (<5 nm) and high thermal stability,[24−26] while the growth of graphene requires a continuous flat substrate.[27,28] Compared with MWCNTs, the synthesis of SWCNTs requires much tougher conditions, and achieving rapid growth of SWCNTs on a graphene substrate is extremely difficult. Attributed to the fact that the carbon atoms in the graphene sheet can dissolve into the metal NPs during the precondition process,[29] which results in the quick sintering of metal NPs on the graphene surface, and the as-grown CNTs on the graphene substrate usually have multiwall numbers and poor graphitization.[16−20,22,23] The introduction of barriers, such as SiO_2[20] and Al_2O_3,[21,23] greatly enhances the catalytic activity for CNT formation; however, the large metal NPs distributed on the barriers are usually effective for MWCNT formation. The one-step CVD growth of SWCNT and graphene for in situ hybrid formation is an interesting idea, but is difficult to be well realized on pure metal substrates.[22] The main problem lies in the unstable catalyst NPs that cannot catalyze the growth of SWCNTs during CVD. Recently, one-step fabrication of G/SWCNT hybrids was reported by using a mixed catalyst.[30−32] However, the strategy involved in these investigations is much more like an in situ mixing of the as-grown graphene and SWCNTs rather than an in situ growth process.

Therefore, exploration of a multifunctional catalyst that can provide small and thermally stable catalyst NPs for the growth of SWCNTs and a uniform substrate for the deposition of graphene layers simultaneously is the key issue for the fabrication of G/SWCNT hybrids.

With respect to the above-mentioned considerations, layered double hydroxides (LDHs) were expected to be a promising multifunctional catalyst for the one-step CVD growth of G/SWCNT hybrids. LDHs, a kind of hydrotalcite-like material composed of positively charged layers and charge-balancing interlayer anions, are a family of smart materials with anticipated compositions and morphologies. The formation of sp^2 carbon materials from LDHs has been a high priority.[33−37] The reason that we selected LDHs as the promising catalyst for the fabrication of G/SWCNT hybrids is that LDHs can offer a well-preserved flake structure as a hard template for graphene deposition, and they also exhibit the ability to produce embedded high-density metal NPs with extraordinary thermal stability for SWCNT formation based on their layered structure at the same time.[31,38−41] In our previous reports, SWCNTs with different structures have been fabricated with LDHs as the catalyst precursor, including entangled SWCNTs,[25] short aligned SWCNTs,[42] and SWCNT-array double helices.[38,43] However, no graphene layers, only CNTs, can be observed in these reports because a growth temperature of no more than 900 °C was used in the CNT formation. Herein, a high-temperature (over 950 °C) CVD process was performed using FeMgAl LDH flakes to achieve the in situ deposition of both SWCNTs and graphene. G/SWCNT hybrids, with SWCNTs grown on the graphene plane being available after the removal of the as-calcined FeMgAl layered double oxide (LDO) flakes. Covalent C−C bonding between the graphene and SWCNTs can be suspected. On the basis of the high surface area, excellent electrical conductivity, and hierarchal porous structure of the G/SWCNT hybrids, the Li−S battery, which is a promising energy storage device with high energy density,[44−46] was selected as a prototype to demonstrate the excellent properties of the G/SWCNT hybrid for advanced energy storage.

RESULTS AND DISCUSSION

Our strategy for the fabrication of G/SWCNT hybrids is illustrated in Scheme 1. FeMgAl LDH flakes served as the 2D lamellar substrates for the high-temperature CVD of graphene with hydrocarbons. The hydrogen that was generated from the decomposition of hydrocarbons simultaneously reduced the LDHs to form Fe NPs with extraordinary thermal stability. Consequently, SWCNTs grew continuously from these Fe NPs with the continuous introduction of hydrocarbons. G/SWCNT hybrids are available after removal of the calcined LDH flakes. The as-fabricated G/SWCNT hybrids were composed of two portions of the G/SWCNT hybrid with

ACSNANO
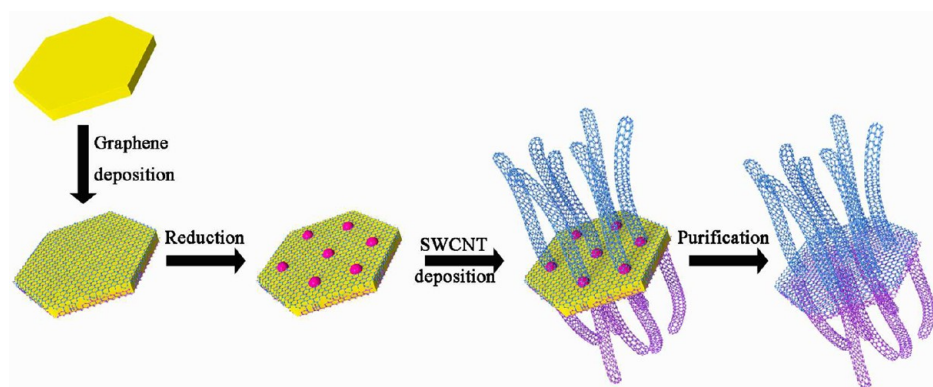
Scheme 1. Schematic illustration of catalytic CVD of G/SWCNT hybrids on LDH flakes.
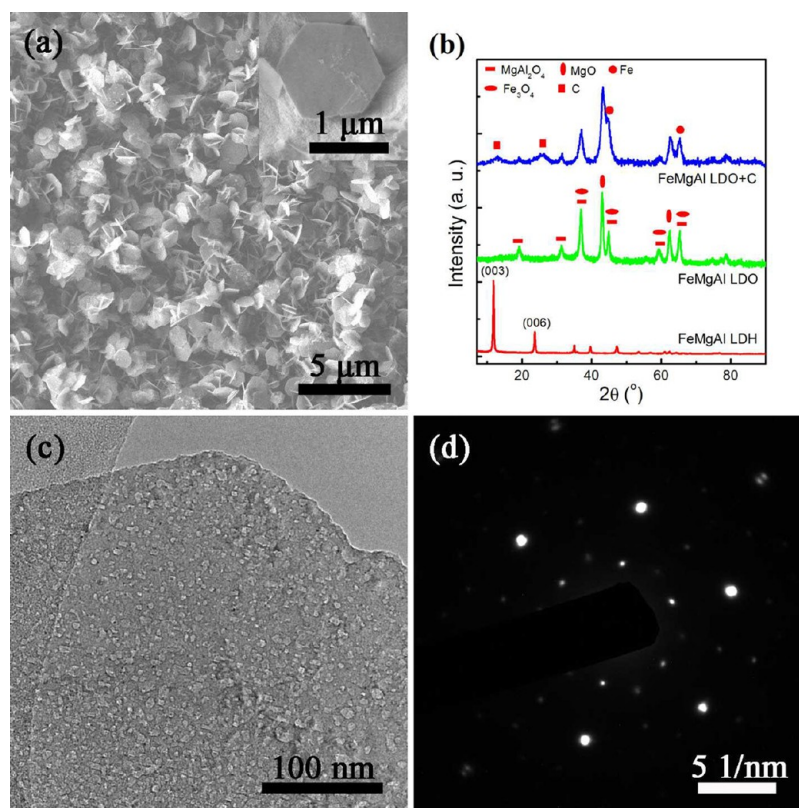

Figure 1. (a) SEM image of the as-prepared FeMgAl LDH flakes. The inset image shows a hexagonal LDH flake. (b) XRD patterns of the FeMgAl LDH and FeMgAl LDO obtained by calcining the FeMgAl LDH at 950 °C for 15 min, and the products after the CVD growth of the G/SWCNT hybrids. (c) TEM image and (d) SAED pattern of the FeMgAl LDO flakes.

their graphene layers stacked together because both sides of the LDH flakes were effective for the deposition of graphene and SWCNTs.

The as-prepared FeMgAl LDHs were well-crystallized hexagonal flakes with a lateral size of *ca.* 1 μm and a thickness of several nanometers (Figure 1a). Calcination of the FeMgAl LDH flakes resulted in dehydration and decarbonization, leading to the formation of corresponding FeMgAl LDO flakes, which were mainly composed of MgO, Fe_3O_4, and $MgAl_2O_4$ (Figure 1b). However, the plate-like structure of the LDHs can be well preserved for the FeMgAl LDO flakes (Figure 1c). The as-obtained FeMgAl LDO flakes had a uniform

structure rather than randomly mixed metal oxides and spinals since a clear hexagonal diffraction pattern was detected by selected area electron diffraction (SAED) (Figure 1d). This can be attributed to the topotactic transformation of the close-packed oxygen layers during the calcination.[47,48]

To reduce the amount of amorphous carbon in the final products, methane was selected as the carbon source for the growth of G/SWCNT hybrids. After the CVD of methane on FeMgAl LDO flakes for 10 min at a high temperature of 950 °C, the as-obtained products showed the morphology of SWCNTs interlinked with flakes (Figure 2a). Graphene with one or two layers was
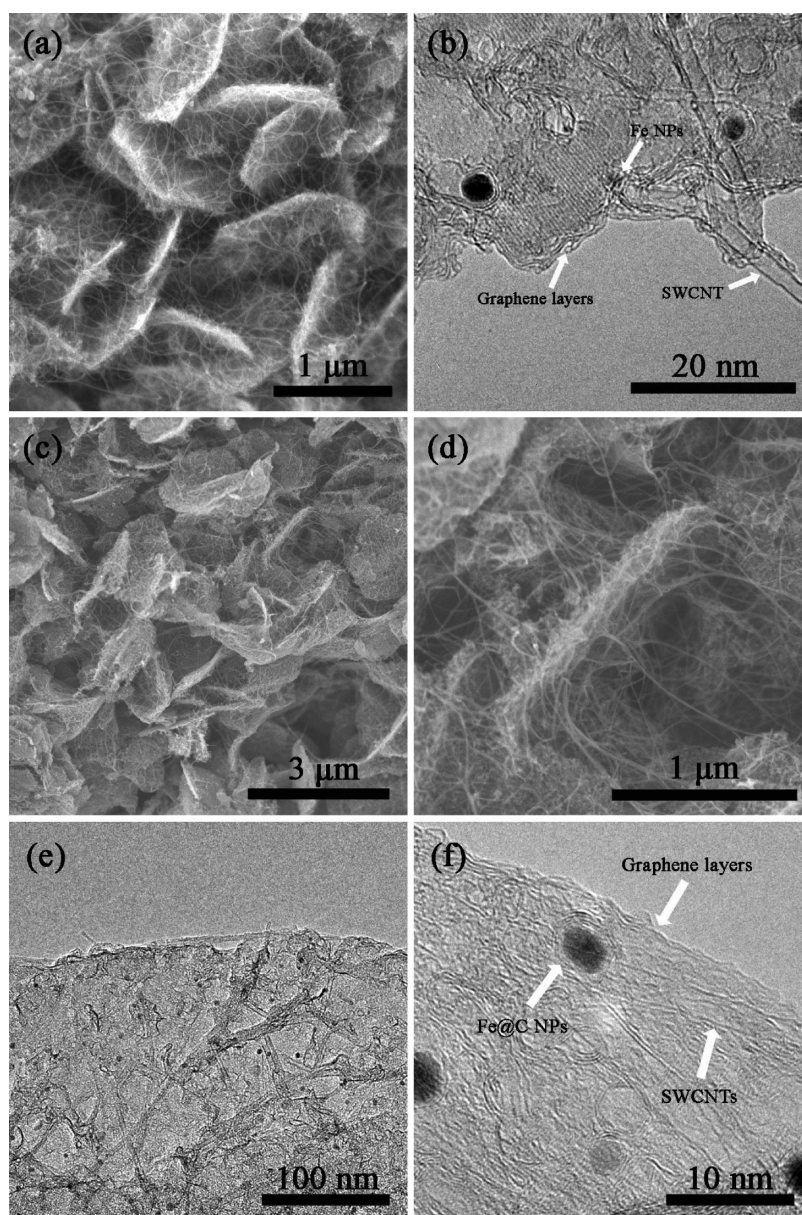
Figure 2. (a) SEM and (b) TEM images of the as-grown G/SWCNT/LDO hybrids; (c, d) SEM image of the as-fabricated G/SWCNT hybrids; (e) TEM and (f) high-resolution TEM image of the G/SWCNT hybrids.

observed on the surface of the LDO flakes, and SWCNTs grown from the small-sized catalyst NPs embedded on the LDO flakes could also be observed (Figure 2b, Figure S2). After the removal of the LDO flakes, the as-obtained G/SWCNT hybrids exhibited a similar inter-linked morphology to that of the G/SWCNT/LDO nano-composites (Figure 2c and d), in which most of SWCNTs grew on the surface of graphene layers on both sides. TEM images revealed that the products were mainly composed of few-layer (<4) graphene and SWCNTs with some graphene layers encapsulating Fe NPs (Fe@C NPs) (Figure 2e and f). On the contrary, when the same CVD procedure was performed on the FeMgAl LDH flakes at a lower temperature of 900 °C, no graphene but only SWCNTs could be detected in the as-grown products (Figure S1a—d). However, similar

G/SWCNT hybrids were available at a higher tempera-ture of 1000 °C (Figure S1e and f). This indicated that a high temperature above 950 °C was essential for the deposition of graphene on FeMgAl LDO flakes from methane, although the growth of SWCNTs on Fe NPs embedded in LDO flakes at temperatures even below 900 °C was possible.[25,38] This can be attributed to the reactivity difference for the catalytic deposition of methane on Fe NPs and LDO flakes. In most cases, good dispersion of few-layer graphene and SWCNTs has always been a key hindrance and a great challenge for their applications. Herein, both the graphene and SWCNTs in the hybrids were effectively distributed in the G/SWCNT hybrid sample: in one aspect, the SWCNTs among graphene layers prevented the stack-ing of graphene sheets; in another aspect, one end of

the as-grown SWCNTs was anchored on the surface of the graphene layers, which inhibited the aggregation of SWCNTs.

A family of strong radial breathing mode (RBM) peaks were detected in the Raman spectra for the G/SWCNT hybrids, indicating the existence of SWCNTs (Figure 3a). In addition, the I_D/I_G ratio for the G/SWCNTs was 0.28, which was larger than that of SWCNTs (0.12). This can be attributed to the defects on the deposited graphene on LDO flakes and the unavoidable defects at the connection spot between graphene and SWCNTs.[49] The thermogravimetric analysis (TGA) curve shown in Figure 3b revealed that the G/SWCNT hybrids had a high carbon purity of 97.5 wt %. Only one sharp weight loss peak was detected with no obvious mass drop before 500 °C in the TGA curve, indicating the hybrids had a small amount of amorphous carbon and the graphene and SWCNTs in the hybrids exhibited similar thermal stability.
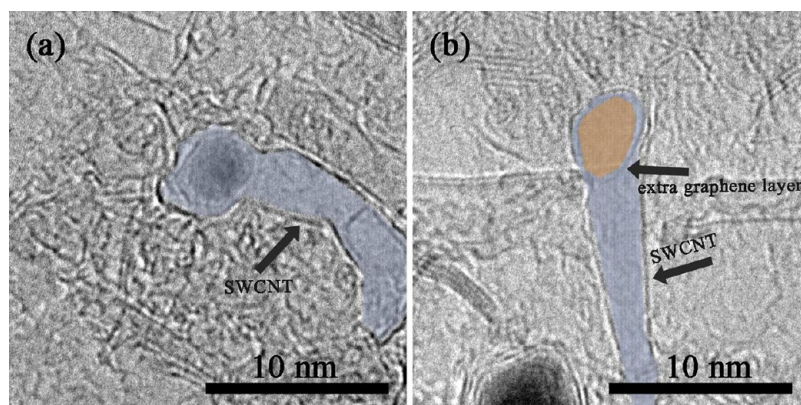
Figure 4a and b shows the interface between SWCNTs and graphene in the G/SWCNT hybrids. The Fe NPs play a decisive role and facilitate the connection between an SWCNT and graphene. At the initial stage of the G/SWCNT hybrid formation, it is suspected that deposition of graphene on the surface of LDO flakes occurred first since only CH_4 was introduced into the reactor chamber. Thus, the generated H_2 from CH_4

decomposition can induce a gradual reduction of FeMgAl LDO flakes to form Fe NPs, the existence of which was demonstrated by the XRD patterns shown in Figure 1b. SWCNTs started to grow on the small-sized Fe NPs along with the continuous deposition of graphene on the LDO flakes. Because of the high solubility of carbon atoms in Fe NPs at such a high temperature (950 °C),[29] the carbon atoms in both the graphene and SWCNTs can be dissolved in the Fe NPs around them. According to the vapor−liquid−solid growth mode, supersaturation of the carbon atoms dissolved in Fe NPs leads to the formation of CNTs. This means that reorganization of carbon atoms takes place in the Fe NPs, which facilitates the effective connections between the SWCNTs and graphene. The morphology of the connection spot between the SWCNT and graphene after the removal of Fe NPs is shown in Figure 4b. A cyclic graphene layer was observed at the end of the SWCNT where it connected with the graphene layer. This was not detected when only SWCNTs were grown if the reaction temperature was low.[25] This morphology is similar to the top view of the proposed G/SWCNT hybrid, in which the extra cyclic graphene layer inside the SWCNT can be attributed to the vacancy on graphene where it connects to the SWCNT. Therefore, a covalent C−C bonding connection can be suspected.

To determine the mass ratio of graphene to SWCNTs in the G/SWCNT hybrids, TGA under a CO_2 atmosphere was adopted. As shown in Figure 5a, the TGA curve of the G/SWCNT hybrids under CO_2 exhibit two distinguished weight-loss periods (stages I−III and III−IV). Residues of the samples at different stages were characterized by TEM. Figure 5b shows the TEM image of the initial G/SWCNT hybrids at stage I, in which SWCNTs and the whole graphene layers are observed. At stage II, it is observed that part of the graphene layer has been oxidized by CO_2 with the obvious migration of Fe NPs (Figure 5c). No graphene layers but a large amount of SWCNT bundles and aggregated Fe NPs were observed at stage III (Figure 5d). This indicated that the Fe
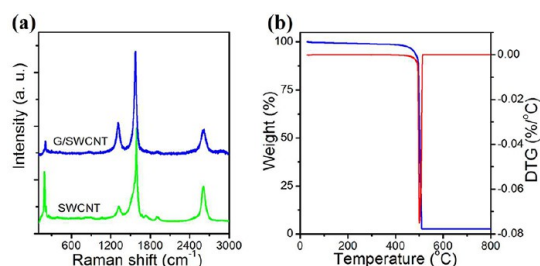
Figure 3. (a) Raman spectra of the SWCNTs obtained at 900 °C and the G/SWCNT hybrids grown from the FeMgAl LDH flakes; (b) TGA curve of the G/SWCNT hybrids under an O_2 atmosphere.

Figure 4. High-resolution TEM images of the G/SWCNT hybrids showing the interface between SWCNTs and graphene (a) before and (b) after the removal of Fe NPs. The SWCNT and extra graphene layer inside the SWCNT are colored and indicated by arrows.
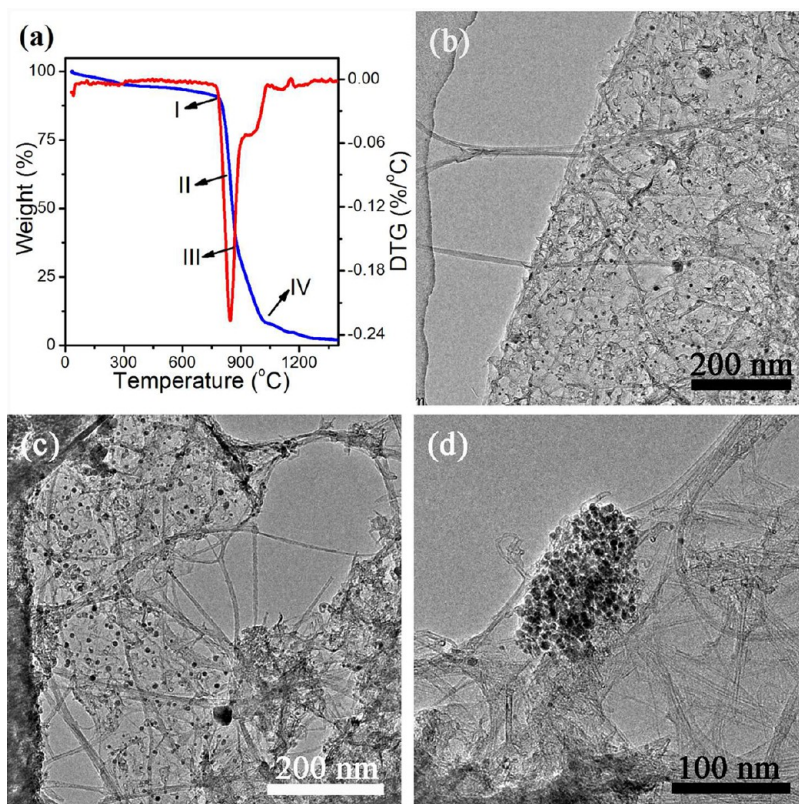
Figure 5. (a) TGA curve of the G/SWCNT hybrids under a CO_2 atmosphere; TEM images of the G/SWCNT hybrids at (b) stage I, (c) stage II, and (d) stage III during the CO_2 oxidation.

NPs selectively catalyze the oxidation of graphene layers during the CO_2 TGA during stages I—III. At stage IV, the residues became brown, indicating the full oxidation of carbon materials in the hybrids. The continuous mass drop after stage IV was attributed to the unstable baseline during TGA. On the other hand, TGA measurement on SWCNTs with a purity of 94.0% was also carried out under a CO_2 atmosphere for comparison (Figures S1a—d, S3). It was observed that below stage III, only a small weight loss of 9.4% occurred for the SWCNTs, most of which corresponds to the burning of carbon layers that encapsulate the Fe NPs (Fe@C NPs). This further demonstrated that the burning of SWCNTs under CO_2 probably occurs only above stage III. Therefore, the two weight-loss periods shown in Figure 5a can be assigned to the oxidation of graphene and SWCNTs in the hybrids by CO_2, respectively. In fact, the thermal stabilities of graphene and SWCNTs do not greatly differ according to their theoretical structure. However, there were *ca.* 2.5 wt % Fe NPs (appeared as Fe@C) on the graphene layers in the as-fabricated hybrids. These Fe NPs are responsible for the enlarged difference in the thermal stability between graphene and SWCNTs in the hybrids and provide the possibility to distinguish them by the TGA profile under CO_2. In addition, the defects on graphene may also contribute to their oxidation reactivity. The mass ratio of graphene to SWCNTs in the as-synthesized G/SWCNTs is

determined as *ca.* 3:2. Note that the yield and length of SWCNTs grown from FeMgAl LDHs are tunable by varying the composition of LDHs and growth parameters.[25,38,42,43,50] Besides, the lateral size of the graphene is controllable in the range of tens of nanometers to several micrometers depending on the size of LDH flakes. The thickness of graphene can also be adjusted through controlling the reaction time. Therefore, the mass ratio of graphene to SWCNTs in the G/SWCNT hybrids is adjustable in a wide range to optimize their performance.

The as-fabricated G/SWCNT hybrids are expected to have a large SSA, high electrical conductivity, excellent structural stability, and abundant porosity, which render them as promising electrode materials for energy storage. Herein, the performance of G/SWCNT hybrids was evaluated as the sulfur host for Li—S batteries. The G/SWCNT-S cathodes prepared through a simple melt-diffusion method showed no obvious morphology change compared with the G/SWCNT hybrids (Figure 6a and b). The S can be distributed uniformly in the G/SWCNT hybrids even with a high incorporation ratio of 60 wt % (Figure 6b—d). No bulk S particles can be found. Both the compartment between the two opposite graphene layers and the internal pore of the SWCNT bundles provide the free space to hold the active S phase (Figure 6d). A strong interaction between the G/SWCNT and S was demonstrated by the
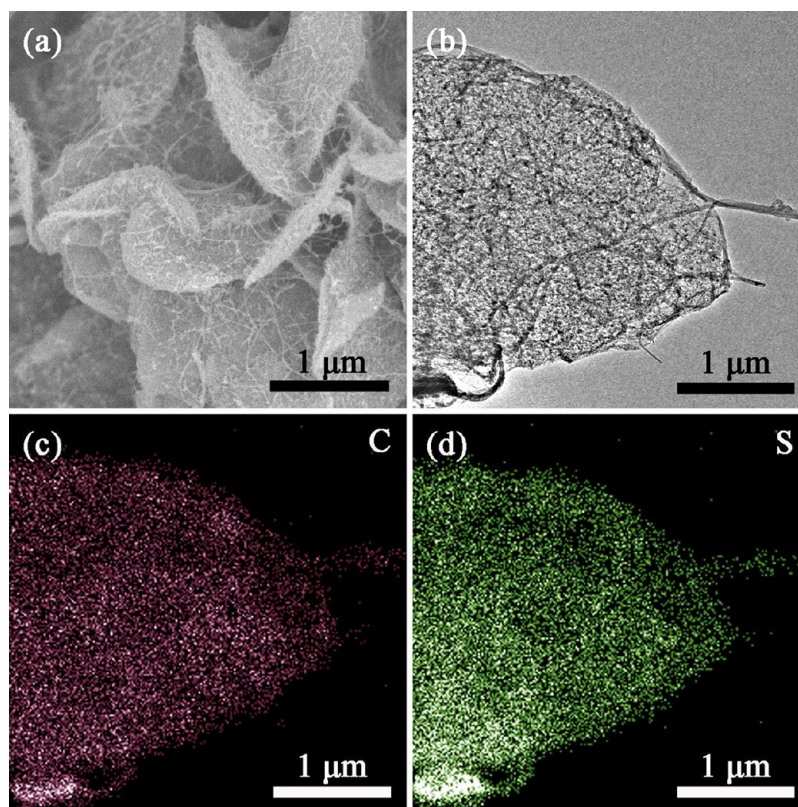
Figure 6. (a) SEM and (b) TEM image of the G/SWCNT-S nanocomposites; (c, d) EDS mapping of the G/SWCNT-S nanocomposites showing the distribution of C and S.

fact that the S in the G/SWNCT-S nanocomposites exhibited a much better thermal stability compared with pure S powders (Figure 7a). No characteristic X-ray diffraction (XRD) peaks of S can be detected for the G/SWNCT-S nanocomposites (Figure 7b), which also indicated a uniform distribution of S in the composite cathode. The G/SWCNT hybrids had a high SSA of 806.2 m^2 g^{-1} calculated by the multipoint Brunauer–Emmett–Teller (BET) method. It reduced to 25.4 m^2 g^{-1} after the incorporation of S. The pore size distribution of the samples was calculated based on the density functional theory (DFT) model. The G/SWCNT hybrids exhibited a large total pore volume of 1.55 cm^3 g^{-1} with pore size distribution concentrated around 8 nm. Most of the pores were filled after the incorporation of S with the total pore volume reduced to 0.087 cm^3 g^{-1} (Figures S4, 7c).

Li–S cells were fabricated to investigate the electrochemical performance of the G/SWCNT-S cathodes. Note that a 3D electroconductive network with excellent conductivity can be constructed with the G/SWCNT hybrids; thus no other conductive agent, such as carbon black, was required for the fabrication of the electrode. During the first four cycles of the cyclic voltammogram (CV) profiles, no obvious changes can be observed for both the anodic/cathodic peaks (Figure 8a), indicating the electrochemical stability of the cathode. The cycling stability of the G/SWCNT-S nanocomposites is illustrated in Figure 8b. An initial reversible capacity of 928 mAh g^{-1} was achieved at the current rate of 1 C, which decreased to *ca.* 530 mAh g^{-1} after 100 cycles with a capacity fading of over 40%. However, with a high current rate of 5 C, the capacity decay was reduced to *ca.* 20% after 100 cycles with an initial value of 822 mAh g^{-1}. In addition, the Coulombic efficiency of the G/SWCNT-S nanocomposites was also increased from 85% at 1 C to 92% for 5 C (Figure 8b). Two discharge plateaus corresponding to the reduction of S to high-order lithium polysulfides and to Li_2S_2 and Li_2S,[45] respectively, were observed for all the discharge curves at different current rates (Figure 8c). At a current rate of 0.5 C, a reversible capacity of *ca.* 1010 mAh g^{-1} was achieved. The capacity decreased gradually with the increased current rate. However, a high reversible capacity of *ca.* 650 mAh g^{-1} can still be preserved even at the very high current rate of 5 C, indicating an excellent rate performance of the G/SWCNT-S nanocomposites (Figure 8d). It is noticed that the capacity corresponding to the first plateaus at higher voltage on the discharge curves, which is contributed by the reduction of S to high-order lithium polysulfides, undergoes no obvious decrease with the increasing current rate. However, the capacity corresponding to the second plateaus at lower voltage on the discharge curves, which is contributed by the further reduction of high-order lithium polysulfides into Li_2S_2 and Li_2S,
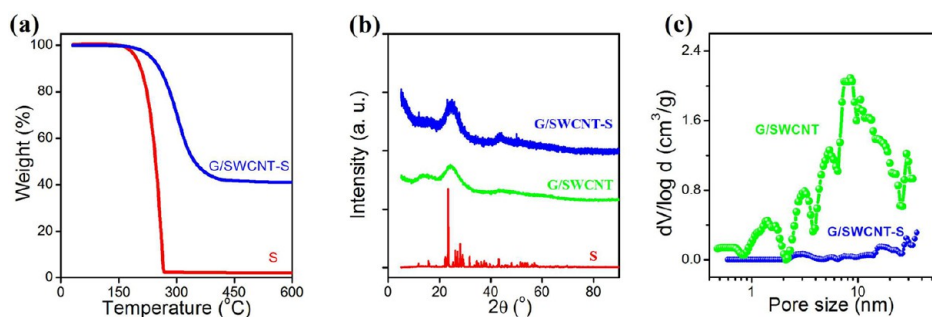
Figure 7. (a) TGA profiles of S and G/SWCNT-S nanocomposites under N_2 atmosphere; (b) XRD patterns of S, G/SWCNT hybrids, and the G/SWCNT-S nanocomposites; (c) pore size distribution of the G/SWCNT hybrids and G/SWCNT-S nanocomposites.
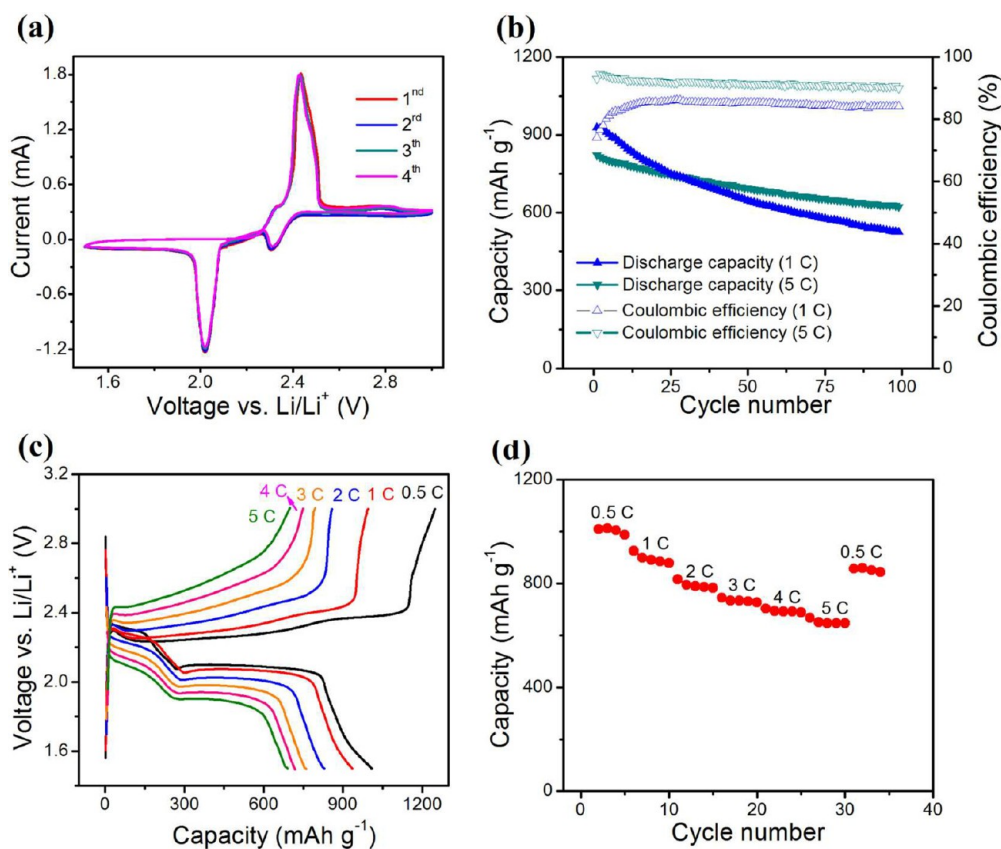

Figure 8. Electrode performance of the G/SWCNT-S nanocomposites for Li−S cells: (a) CV profiles; (b) cycling stability; (c) galvanostatic charge−discharge curves at different current rates; (d) rate performance.

decreases greatly with increasing the current rate. As shown in Figure 8c, the S in the G/SWCNT-S cathodes can be fully utilized at every current rate. However, the reduction of high-order lithium polysulfides to Li_2S_2 and Li_2S is partially hindered at high current rate due to the fast electron transfer. Polarization of the cathode materials is also observed due to their increasing charging-voltage and decreasing discharging-voltage with the increasing current rate. The recovery of a reversible capacity of *ca.* 860 mAh g^{-1} was achieved at 0.5 C following the charge/discharge process at the high current rate of 5 C (Figure 8d).

Recent advances in nanocarbon−sulfur cathodes have demonstrated enhanced capacity and stability of Li−S batteries. For instance, mesoporous carbons have been demonstrated to be an excellent cathode material for Li−S batteries.[45,51−53] However, the high-rate performance of Li−S cells based on mesoporous carbons is restricted due to their limited electrical conductivity. Recently, nanocarbon materials with improved electrical conductivity, such as graphene and MWCNTs, have been widely used as cathode materials for Li−S batteries.[54−59] However, the graphene materials used were always prepared by chemically derived processes and still showed poor conductivity due to

their severe structural defects introduced during the exfoliation and reduction processes.[55−59] The electrochemical performance of CNTs as the cathode materials for Li−S batteries was always limited due to the poor S-storage ability of MWCNTs.[54] The combination of CVD-grown graphene and SWCNTs into hybrid materials renders their promising applications as cathodes with high-rate performance. On one hand, the internal spaces between the two stacked graphene layers and among the SWCNT bundles contributed mesopores with sizes of *ca.* 8 nm for the G/SWCNT hybrids, which offers the space for S storage. The shuttling effect in the confined space of the mesopores can be inhibited.[44,52,60] On the other hand, a good electrical conductivity can be expected for the G/SWCNT hybrids. The G/SWCNT hybrids were compressed at 5 MPa into a disk with a diameter of 13 mm and a thickness of 150 μm to determine their electrical conductivity (Figure S5). The conductivity was measured as 3130 S cm^{-1} by the four-probe technique, which was much higher than that of the chemically derived graphene paper (60−350 S cm^{-1})[12,61] and SWCNT paper (100−700 S cm^{-1}).[62,63] Electrochemical impedance spectroscopy was measured for the G/SWCNT-S electrode to further demonstrate the high electrical conductivity of the G/SWCNT hybrids (Figure S6). It is obvious that the charge transfer resistance of the G/SWCNT-S electrode, which corresponds to the diameter of the semicircle at high frequencies, is much lower than that when graphene or even polyacrylonitrile-coated graphene was used as the electrode materials.[56,64] The high electrical conductivity of the CVD-grown graphene and SWCNTs as well as the effective connections between the SWCNTs

and graphene facilitated the construction of the high electrical conductive network to ensure a fast electron transfer, which greatly contributes to the extraordinary rate performance of the G/SWCNT-S cathode. The cathode of the Li−S battery serves as a prototype application to shed light on the combination of graphene and SWCNTs into advanced hybrid materials with unexpected properties.

CONCLUSIONS

In summary, direct growth of G/SWCNT hybrids was successfully achieved through one-step CVD of methane on FeMgAl LDO flakes at a high temperature above 950 °C. The LDO surface served as the substrate for graphene deposition, and the thermally stable Fe NPs embedded on the LDO flakes catalyzed the growth of SWCNTs and facilitated the effective connection between SWCNTs and graphene. The mass ratio of graphene to SWCNTs in the hybrids was determined to be 3:2. When S was incorporated into the hybrids as electrode materials for Li−S batteries, a 3D electrical conductive net could be constructed by the hybrids themselves, which ensured the fabrication of conductive agent-free G/SWCNT-S electrodes. The G/SWCNT-S nanocomposites exhibited excellent rate performance for Li−S batteries. A reversible capacity of 928 mAh g^{-1} can be achieved at 1 C with a S loading amount of 60%. At a very high current density of 5 C, a capacity as high as *ca.* 650 mAh g^{-1} can be preserved even after 100 cycles with a Coulombic efficiency of *ca.* 92%. The strategy is generally applicable for the fabrication of the proposed theoretical G/SWCNT hybrids to fully explore their potentials and extend the applications of graphene and SWCNTs.

EXPERIMENTAL SECTION

Catalyst Preparation. The FeMgAl LDH flakes were prepared using a urea-assisted co-precipitation reaction. Fe(NO$_3$)$_3$·9H$_2$O, Mg(NO$_3$)$_2$·9H$_2$O, Al(NO$_3$)$_3$·9H$_2$O, and urea were dissolved in deionized water (1000 mL) with [Fe^{3+}] + [Mg^{2+}] + [Al^{3+}] = 0.15 mol L^{-1}, n(Fe):n(Mg):n(Al) = 0.4:3:1, and [urea] = 3.0 mol L^{-1}. The solution was kept at 94 °C under continuous magnetic stirring for 12 h in a 2000 mL flask (equipped with a reflux condenser) under an ambient atmosphere. The as-obtained suspension was then filtered, and the residue was washed by deionized water. After freeze-drying, the final products were ground into brown-yellow powders, which were used as the catalyst for the growth of the G/SWCNT hybrids.

Synthesis of G/SWCNT Hybrids. The synthesis of G/SWCNT hybrids was carried out using a high-temperature catalytic CVD. Typically, the FeMgAl LDH flakes were sprayed uniformly into a quartz boat, which was then placed at the center of a horizontal quartz tube inserted into a furnace at atmospheric pressure. The furnace was then heated under an Ar atmosphere with a flow rate of 400 mL min^{-1}. On reaching 950 °C, CH$_4$ (400 mL min^{-1}) was introduced into the reactor for 10 min. After that, the furnace was cooled to room temperature under Ar flow. Similar processes were also performed at 900 and 1000 °C. The as-obtained products were treated with an HCl (1 mol L^{-1}) aqueous solution at 80 °C for 3 h and an NaOH (6 mol L^{-1}) aqueous

solution at 150 °C for 6 h, subsequently, to remove the FeMgAl LDO flakes. After filtering and drying, the samples were further treated with CO$_2$ (20%) and Ar (80%) at 750 °C for 30 min followed by an HCl treatment at 80 °C for 1 h to further remove iron in the samples. The as-obtained products were filtered, washed, and freeze-dried for further characterizations.

Fabrication of G/SWCNT-S Nanocomposites. The G/SWCNT-S nanocomposites were fabricated following a typical melt-diffusion strategy. The G/SWCNT hybrids were first mixed with S powder with a mass ratio of 1:2 by milling. The mixture was then placed in a sealed flask at 155 °C for 24 h to incorporate the S into the G/SWCNT hybrids.

Characterizations. The morphology of the samples was characterized by a JSM 7401F (JEOL Ltd., Tokyo, Japan) SEM operated at 3.0 kV and a JEM 2010 (JEOL Ltd., Tokyo, Japan) TEM operated at 120.0 kV. X-ray diffraction patterns were recorded on a Bruker D8 Advance diffractometer at 40.0 kV and 120 mA with Cu Kα radiation. The pore-size distribution and BET specific surface area of the samples were measured by N$_2$ adsorption/desorption using an Autosorb-iQ2-MP-C system. Energy dispersive spectroscopy (EDS) analysis was performed using a JEM 2010 TEM equipped with an Oxford Instrument energy dispersive spectrometer, and the acceleration voltage applied was 120.0 kV. Raman spectra were recorded with He−Ne laser excitation at 633 nm using a Horiba Jobin Yvon LabRAM HR800 Raman spectrometer. The TGA was carried out on the

samples using a TGA/DSC1 STAR^e system under an O_2, CO_2, and N_2 atmosphere, respectively. The resistance measurements of the G/SWCNT hybrid disk were performed using the KDY-1 four-probe technique.

G/SWCNT-S Cathode for Li—S Battery. Two-electrode cells using standard 2025 coil-type cells were constructed to evaluate the electrochemical performance of the G/SWCNT hybrids as the cathode material for Li—S batteries. The G/SWCNT-S cathode slurry was prepared by mixing 90% of the G/SWCNT-S nanocomposites and 10% of the poly(vinylidene fluoride) binder in an N-methylpyrrolidone solvent dispersant. The positive electrodes were fabricated through coating the slurry on aluminum foil and drying at 60 °C for 24 h. a 1 mol L^{-1} lithium bis-(trifluoromethanesulfonyl)imide solution in 1:1 (v/v) 1,3-dioxolane/1,2-dimethoxyethane was used as the electrolyte. Lithium metal foil was used as the anode, and polypropylene membranes from Celgard Inc. were used as the separators. The coin cells were tested in galvanostatic mode at various currents within a voltage range of 1.5—3.0 V using a Neware multichannel battery cycler. The CV measurements were performed on a Solartron 1470E electrochemical workstation at a scan rate of 0.1 mV s^{-1}. A current density of 1672 mA g^{-1} (1 C) equivalent to full discharge or charge in one hour was applied in both current sweep directions. The capacities were calculated corresponding to the mass of sulfur.

Conflict of Interest: The authors declare no competing financial interest.

Supporting Information Available: SEM and TEM images of the samples obtained at 900 and 1000 °C; TEM images of FeMgAl LDO flakes and the G/SWCNT/LDO nanocomposites after CVD growth; comparison of the TGA curves of G/SWCNT hybrids and SWCNTs under CO_2 atmosphere; N_2 adsorption—desorption isotherms of the G/SWCNT hybrids and G/SWCNT-S nanocomposites, and a photograph of the G/SWCNT hybrid disk. This material is available free of charge *via* the Internet at http://pubs.acs.org.

REFERENCES AND NOTES

1. Zhou, W. Y.; Bai, X. D.; Wang, E. G.; Xie, S. S. Synthesis, Structure, and Properties of Single-Walled Carbon Nanotubes. *Adv. Mater.* **2009**, *21*, 4565–4583.
2. Ajayan, P. M.; Zhou, O. Z. Applications of Carbon Nanotubes. *Top. Appl. Phys.* **2001**, *80*, 391–425.
3. Endo, M.; Strano, M. S.; Ajayan, P. M. Potential Applications of Carbon Nanotubes. *Top. Appl. Phys.* **2008**, *111*, 13–61.
4. Xu, L.; Wei, N.; Zheng, Y.; Fan, Z.; Wang, H.-Q.; Zheng, J.-C. Graphene-Nanotube 3D Networks: Intriguing Thermal and Mechanical Properties. *J. Mater. Chem.* **2011**, *22*, 1435–1444.
5. Dimitrakakis, G. K.; Tylianakis, E.; Froudakis, G. E. Pillared Graphene: A New 3-D Network Nanostructure for Enhanced Hydrogen Storage. *Nano Lett.* **2008**, *8*, 3166–3170.
6. Geim, A. K.; Novoselov, K. S. The Rise of Graphene. *Nat. Mater.* **2007**, *6*, 183–191.
7. Hong, T. K.; Lee, D. W.; Choi, H. J.; Shin, H. S.; Kim, B.-S. Transparent, Flexible Conducting Hybrid Multi layer Thin Films of Multiwalled Carbon Nanotubes with Graphene Nanosheets. *ACS Nano* **2010**, *4*, 3861–3868.
8. Byon, H. R.; Lee, S. W.; Chen, S.; Hammond, P. T.; Shao-Horn, Y. Thin Films of Carbon Nanotubes and Chemically Reduced Graphenes for Electrochemical Micro-Capacitors. *Carbon* **2011**, *49*, 457–467.
9. Liu, Y.; Liu, Y.; Feng, H.; Wu, Y.; Joshi, L.; Zeng, X.; Li, J. Layer-by-Layer Assembly of Chemical Reduced Graphene and Carbon Nanotubes for Sensitive Electrochemical Immunoassay. *Biosens. Bioelectron.* **2012**, *35*, 63–68.
10. Yu, D. S.; Dai, L. M. Self-Assembled Graphene/Carbon Nanotube Hybrid Films for Supercapacitors. *J. Phys. Chem. Lett.* **2010**, *1*, 467–470.
11. Peng, L. W.; Feng, Y. Y.; Lv, P.; Lei, D.; Shen, Y. T.; Li, Y.; Feng, W. Transparent, Conductive, and Flexible Multiwalled Carbon Nanotube/Graphene Hybrid Electrodes with Two Three-Dimensional Microstructures. *J. Phys. Chem. C* **2012**, *116*, 4970–4978.
12. Shao, J. J.; Lv, W.; Guo, Q. G.; Zhang, C.; Xu, Q.; Yang, Q. H.; Kang, F. Y. Hybridization of Graphene Oxide and Carbon Nanotubes at the Liquid/Air Interface. *Chem. Commun.* **2012**, *48*, 3706–3708.
13. Bon, S. B.; Valentini, L.; Kenny, J. M.; Peponi, L.; Verdejo, R.; Lopez-Manchado, M. A. Electrodeposition of Transparent and Conducting Graphene/Carbon Nanotube Thin Films. *Phys. Status Solidi A* **2010**, *207*, 2461–2466.
14. Tung, V. C.; Chen, L.-M.; Allen, M. J.; Wassei, J. K.; Nelson, K.; Kaner, R. B.; Yang, Y. Low-Temperature Solution Processing of Graphene-Carbon Nanotube Hybrid Materials for High-Performance Transparent Conductors. *Nano Lett.* **2009**, *9*, 1949–1955.
15. Cai, D.; Song, M.; Xu, C. Highly Conductive Carbon-Nanotube/Graphite-Oxide Hybrid Films. *Adv. Mater.* **2008**, *20*, 1706–1709.
16. Fan, Z. J.; Yan, J.; Zhi, L.; Zhang, Q.; Wei, T.; Feng, J.; Zhang, M.; Qian, W.; Wei, F. A Three-Dimensional Carbon Nanotube/Graphene Sandwich and Its Application as Electrode in Supercapacitors. *Adv. Mater.* **2010**, *22*, 3723–3728.
17. Fan, Z. J.; Yan, J.; Wei, T.; Ning, G. Q.; Zhi, L.-J.; Liu, J. C.; Cao, D. X.; Wang, G.-L.; Wei, F. Nanographene-Constructed Carbon Nanofibers Grown on Graphene Sheets by Chemical Vapor Deposition: High-Performance Anode Materials for Lithium Ion Batteries. *ACS Nano* **2011**, *5*, 2787–2794.
18. Chen, S.; Chen, P.; Wang, Y. Carbon Nanotubes Grown *In Situ* on Graphene Nanosheets as Superior Anodes for Li-Ion Batteries. *Nanoscale* **2011**, *3*, 4323–4329.
19. Zhang, L. L.; Xiong, Z. G.; Zhao, X. S. Pillaring Chemically Exfoliated Graphene Oxide with Carbon Nanotubes for Photocatalytic Degradation of Dyes under Visible Light Irradiation. *ACS Nano* **2010**, *4*, 7030–7036.
20. Du, F.; Yu, D. S.; Dai, L. M.; Ganguli, S.; Varshney, V.; Roy, A. K. Preparation of Tunable 3D Pillared Carbon Nanotube-Graphene Networks for High-Performance Capacitance. *Chem. Mater.* **2011**, *23*, 4810–4816.
21. Li, S.; Luo, Y.; Lv, W.; Yu, W.; Wu, S.; Hou, P.; Yang, Q.; Meng, Q.; Liu, C.; Cheng, H. M. Vertically Aligned Carbon Nanotubes Grown on Graphene Paper as Electrodes in Lithium-Ion Batteries and Dye-Sensitized Solar Cells. *Adv. Energy Mater.* **2011**, *1*, 486–490.
22. Paul, R. K.; Ghazinejad, M.; Penchev, M.; Lin, J.; Ozkan, M.; Ozkan, C. S. Synthesis of a Pillared Graphene Nanostructure: A Counterpart of Three-Dimensional Carbon Architectures. *Small* **2010**, *6*, 2309–2313.
23. Lee, D. H.; Kim, J. E.; Han, T. H.; Hwang, J. W.; Jeon, S.; Choi, S.-Y.; Hong, S. H.; Lee, W. J.; Ruoff, R. S.; Kim, S. O. Versatile Carbon Hybrid Films Composed of Vertical Carbon Nanotubes Grown on Mechanically Compliant Graphene Films. *Adv. Mater.* **2010**, *22*, 1247–1252.
24. Zhang, Q.; Huang, J. Q.; Zhao, M. Q.; Qian, W. Z.; Wei, F. Carbon Nanotube Mass Production: Principles and Processes. *ChemSusChem* **2011**, *4*, 864–889.
25. Zhao, M. Q.; Zhang, Q.; Jia, X. L.; Huang, J. Q.; Zhang, Y. H.; Wei, F. Hierarchical Composites of Single/Double-Walled Carbon Nanotubes Interlinked Flakes from Direct Carbon Deposition on Layered Double Hydroxides. *Adv. Funct. Mater.* **2010**, *20*, 677–685.
26. Tessonnier, J. P.; Su, D. S. Recent Progress on the Growth Mechanism of Carbon Nanotubes: A Review. *ChemSusChem* **2011**, *4*, 824–847.
27. Chen, Z.; Ren, W.; Gao, L.; Liu, B.; Pei, S.; Cheng, H.-M. Three-Dimensional Flexible and Conductive Interconnected Graphene Networks Grown by Chemical Vapour Deposition. *Nat. Mater.* **2011**, *10*, 424–428.
28. Li, X.; Cai, W.; An, J.; Kim, S.; Nah, J.; Yang, D.; Piner, R.; Velamakanni, A.; Jung, I.; Tutuc, E.; Banerjee, S. K.; Colombo, L.; Ruoff, R. S. Large-Area Synthesis of High-Quality and Uniform Graphene Films on Copper Foils. *Science* **2009**, *324*, 1312–1314.
29. Rinaldi, A.; Tessonnier, J.-P.; Schuster, M. E.; Blume, R.; Girgsdies, F.; Zhang, Q.; Jacob, T.; Hamid, S. B. A.; Su, D. S.;

Schloegl, R. Dissolved Carbon Controls the Initial Stages of Nanocarbon Growth. *Angew. Chem., Int. Ed.* **2011**, *50*, 3313–3317.

30. Wu, Y. P.; Zhang, T. F.; Zhang, F.; Wang, Y.; Ma, Y. F.; Huang, Y.; Liu, Y. Y.; Chen, Y. S. *In Situ* Synthesis of Graphene/Single-Walled Carbon Nanotube Hybrid Material by Arc-Discharge and Its Application in Supercapacitors. *Nano Energy* **2012**, *1*, 820–827.

31. Zhu, X.; Ning, G.; Fan, Z.; Gao, J.; Xu, C.; Qian, W.; Wei, F. One-Step Synthesis of a Graphene-Carbon Nanotube Hybrid Decorated by Magnetic Nanoparticles. *Carbon* **2012**, *50*, 2764–2771.

32. Wang, Y.; Wu, Y.; Huang, Y.; Zhang, F.; Yang, X.; Ma, Y.; Chen, Y. Preventing Graphene Sheets from Restacking for High-Capacitance Performance. *J. Phys. Chem. C* **2011**, *115*, 23192–23197.

33. Zhao, M. Q.; Zhang, Q.; Huang, J. Q.; Wei, F. Hierarchical Nanocomposites Derived from Nanocarbons and Layered Double Hydroxides - Properties, Synthesis, and Applications. *Adv. Funct. Mater.* **2012**, *22*, 675–694.

34. Debecker, D. P.; Gaigneaux, E. M.; Busca, G. Exploring, Tuning, and Exploiting the Basicity of Hydrotalcites for Applications in Heterogeneous Catalysis. *Chem.—Eur. J.* **2009**, *15*, 3920–3935.

35. Guo, X. X.; Zhang, F. Z.; Evans, D. G.; Duan, X. Layered Double Hydroxide Films: Synthesis, Properties and Applications. *Chem. Commun.* **2010**, *46*, 5197–5210.

36. Xu, Z. P.; Zhang, J.; Adebajo, M. O.; Zhang, H.; Zhou, C. H. Catalytic Applications of Layered Double Hydroxides and Derivatives. *Appl. Clay Sci.* **2011**, *53*, 139–150.

37. Yan, D. P.; Lu, J.; Wei, M.; Evans, D. G.; Duan, X. Recent Advances in Photofunctional Guest/Layered Double Hydroxide Host Composite Systems and Their Applications: Experimental and Theoretical Perspectives. *J. Mater. Chem.* **2011**, *21*, 13128–13139.

38. Zhao, M. Q.; Zhang, Q.; Zhang, W.; Huang, J. Q.; Zhang, Y.; Su, D. S.; Wei, F. Embedded High Density Metal Nanoparticles with Extraordinary Thermal Stability Derived from Guest-Host Mediated Layered Double Hydroxides. *J. Am. Chem. Soc.* **2010**, *132*, 14739–14741.

39. Ruemmeli, M. H.; Kramberger, C.; Grueneis, A.; Ayala, P.; Gemming, T.; Buechner, B.; Pichler, T. On the Graphitization Nature of Oxides for the Formation of Carbon Nanostructures. *Chem. Mater.* **2007**, *19*, 4105–4107.

40. Ruemmeli, M. H.; Bachmatiuk, A.; Scott, A.; Boerrnert, F.; Warner, J. H.; Hoffman, V.; Lin, J. H.; Cuniberti, G.; Buechner, B. Direct Low-Temperature Nanographene CVD Synthesis over a Dielectric Insulator. *ACS Nano* **2010**, *4*, 4206–4210.

41. Ning, G.; Fan, Z.; Wang, G.; Gao, J.; Qian, W.; Wei, F. Gram-Scale Synthesis of Nanomesh Graphene with High Surface Area and Its Application in Supercapacitor Electrodes. *Chem. Commun.* **2011**, *47*, 5976–5978.

42. Zhao, M. Q.; Tian, G. L.; Zhang, Q.; Huang, J. Q.; Nie, J. Q.; Wei, F. Preferential Growth of Short Aligned, Metallic-Rich Single-Walled Carbon Nanotubes from Perpendicular Layered Double Hydroxide Film. *Nanoscale* **2012**, *4*, 2470–2477.

43. Zhao, M. Q.; Zhang, Q.; Tian, G. L.; Huang, J. Q.; Wei, F. Space Confinement and Rotation Stress Induced Self-Organization of Double-Helix Nanostructure: A Nanotube Twist with a Moving Catalyst Head. *ACS Nano* **2012**, *6*, 4520–4529.

44. Ji, X.; Lee, K. T.; Nazar, L. F. A Highly Ordered Nanostructured Carbon-Sulphur Cathode for Lithium-Sulphur Batteries. *Nat. Mater.* **2009**, *8*, 500–506.

45. Bruce, P. G.; Freunberger, S. A.; Hardwick, L. J.; Tarascon, J.-M. Li-O$_2$ and Li-S Batteries with High Energy Storage. *Nat. Mater.* **2012**, *11*, 19–29.

46. Ji, X.; Nazar, L. F. Advances in Li-S Batteries. *J. Mater. Chem.* **2010**, *20*, 9821–9826.

47. Sun, J.; Liu, H.; Chen, X.; Evans, D. G.; Yang, W.; Duan, X. Synthesis of Graphene Nanosheets with Good Control over the Number of Layers within the Two-Dimensional Galleries of Layered Double Hydroxides. *Chem. Commun.* **2012**, *48*, 8126–8128.

48. Li, C.; Wang, L.; Wei, M.; Evans, D. G.; Duan, X. Large Oriented Mesoporous Self-Supporting Ni-Al Oxide Films Derived from Layered Double Hydroxide Precursors. *J. Mater. Chem.* **2008**, *18*, 2666–2672.

49. Saito, R.; Dresselhaus, G.; Dresselhaus, M. S. Topological Defects in Large Fullerenes. *Chem. Phys. Lett.* **1992**, *195*, 537–542.

50. Zhao, M. Q.; Zhang, Q.; Huang, J. Q.; Nie, J. Q.; Wei, F. Layered Double Hydroxides as Catalysts for the Efficient Growth of High Quality Single-Walled Carbon Nanotubes in a Fluidized Bed Reactor. *Carbon* **2010**, *48*, 3260–3270.

51. Jayaprakash, N.; Shen, J.; Moganty, S. S.; Corona, A.; Archer, L. A. Porous Hollow Carbon@Sulfur Composites for High-Power Lithium-Sulfur Batteries. *Angew. Chem., Int. Ed.* **2011**, *50*, 5904–5908.

52. Schuster, J.; He, G.; Mandlmeier, B.; Yim, T.; Lee, K. T.; Bein, T.; Nazar, L. F. Spherical Ordered Mesoporous Carbon Nanoparticles with High Porosity for Lithium-Sulfur Batteries. *Angew. Chem., Int. Ed.* **2012**, *51*, 3591–3595.

53. Wang, D. W.; Zhou, G. M.; Li, F.; Wu, K. H.; Lu, G. Q.; Cheng, H. M.; Gentle, I. R. A Microporous-Mesoporous Carbon with Graphitic Structure for a High-Rate Stable Sulfur Cathode in Carbonate Solvent-Based Li-S Batteries. *Phys. Chem. Chem. Phys.* **2012**, *14*, 8703–8710.

54. Guo, J.; Xu, Y.; Wang, C. Sulfur-Impregnated Disordered Carbon Nanotubes Cathode for Lithium-Sulfur Batteries. *Nano Lett.* **2011**, *11*, 4288–4294.

55. Ji, L.; Rao, M.; Zheng, H.; Zhang, L.; Li, Y.; Duan, W.; Guo, J.; Cairns, E. J.; Zhang, Y. Graphene Oxide as a Sulfur Immobilizer in High Performance Lithium/Sulfur Cells. *J. Am. Chem. Soc.* **2011**, *133*, 18522–18525.

56. Wang, J. Z.; Lu, L.; Choucair, M.; Stride, J. A.; Xu, X.; Liu, H. K. Sulfur-Graphene Composite for Rechargeable Lithium Batteries. *J. Power Sources* **2011**, *196*, 7030–7034.

57. Evers, S.; Nazar, L. F. Graphene-Enveloped Sulfur in a One Pot Reaction: A Cathode with Good Coulombic Efficiency and High Practical Sulfur Content. *Chem. Commun.* **2012**, *48*, 1233–1235.

58. Wang, H. L.; Yang, Y.; Liang, Y. Y.; Robinson, J. T.; Li, Y. G.; Jackson, A.; Cui, Y.; Dai, H. J. Graphene-Wrapped Sulfur Particles as a Rechargeable Lithium-Sulfur Battery Cathode Material with High Capacity and Cycling Stability. *Nano Lett.* **2011**, *11*, 2644–2647.

59. Zheng, G. Y.; Yang, Y.; Cha, J. J.; Hong, S. S.; Cui, Y. Hollow Carbon Nanofiber-Encapsulated Sulfur Cathodes for High Specific Capacity Rechargeable Lithium Batteries. *Nano Lett.* **2011**, *11*, 4462–4467.

60. Demir-Cakan, R.; Morcrette, M.; Nouar, F.; Davoisne, C.; Devic, T.; Gonbeau, D.; Dominko, R.; Serre, C.; Ferey, G.; Tarascon, J.-M. Cathode Composites for Li-S Batteries *via* the Use of Oxygenated Porous Architectures. *J. Am. Chem. Soc.* **2011**, *133*, 16154–16160.

61. Chen, H.; Mueller, M. B.; Gilmore, K. J.; Wallace, G. G.; Li, D. Mechanically Strong, Electrically Conductive, and Biocompatible Graphene Paper. *Adv. Mater.* **2008**, *20*, 3557–3561.

62. Ng, S. H.; Wang, J.; Guo, Z. P.; Wang, G. X.; Liu, H. K. Single Wall Carbon Nanotube Paper as Anode for Lithium-Ion Battery. *Electrochim. Acta* **2005**, *51*, 23–28.

63. Zhang, D.; Ryu, K.; Liu, X.; Polikarpov, E.; Ly, J.; Tompson, M. E.; Zhou, C. Transparent, Conductive, and Flexible Carbon Nanotube Films and Their Application in Organic Light-Emitting Diodes. *Nano Lett.* **2006**, *6*, 1880–1886.

64. Yin, L.; Wang, J.; Lin, F.; Yang, J.; Nuli, Y. Polyacrylonitrile/Graphene Composite as a Precursor to a Sulfur-Based Cathode Material for High-Rate Rechargeable Li—S Batteries. *Energy Environ. Sci.* **2012**, *5*, 6966–6972.